Materials Advances

PAPER

View Article Online
View Journal | View Issue

Cite this: *Mater. Adv.*, 2023, 4, 3654

High-performance flexible supercapacitors based on potassium nickel(II) hexacyanoferrates(III) nanoparticles on carbon cloth as an electrode material

L. M. Samyn,[a] T. S. Lessa,[a] R. Suresh Babu, *[a] A. Kalaivani,[b] T. M. Barbosa[a] and A. L. F. de Barros [a]

Received 8th May 2023,
Accepted 17th July 2023

DOI: 10.1039/d3ma00219e

rsc.li/materials-advances

In this work, we report the synthesis of three-dimensional open-framework tunnels based on inorganic metal coordination compounds, such as potassium nickel(II) hexacyanoferrate(III) nanoparticles (PNHCF-NPs) by the co-precipitation method. The nanostructured material was characterized using various techniques, such as UV-Vis, FTIR, XPS, FESEM, EDS, and TEM. The prepared PNHCF-NPs were coated on carbon cloth and named PNHCF-NPs@CC. The electrochemical properties of PNHCF-NPs@CC were evaluated using cyclic voltammetry, galvanostatic charge–discharge, and electrochemical impedance spectroscopy techniques. In a 3-electrode cell configuration, PNHCF-NPs@CC electrode demonstrated high capacitance of 198.6 F g^{-1} (Na_2SO_4) and 168.8 F g^{-1} (K_2SO_4) at 0.4 A g^{-1}, excellent rate performance of 88 F g^{-1} (Na_2SO_4) F g^{-1} and 89 F g^{-1} (K_2SO_4), even at 4 A g^{-1}, and outstanding cyclic stability with ∼94% capacitance retention after 1000 cycles at 0.4 A g^{-1} for both electrolytes. The PNHCF-NP@CC hybrid showed high mechanical flexibility, superior electrical conductivity, and remarkably improved electrochemical capacitance, rendering it a promising flexible electrode material for use in high-performance supercapacitors.

Introduction

The rapid growth of miniature electronic devices and hybrid electric vehicles, the ever-increasing demand for clean and renewable energy sources, and the growing concern for the environment have encouraged intensive efforts to explore advanced energy storage and conversion devices.[1,2] Over the last decade, efforts have been made to develop flexible energy storage devices, such as batteries, supercapacitors, and solar cells.[3–8] Supercapacitors (SCs) are energy storage devices that present power density higher than batteries and energy density superior to conventional capacitors. These advantages have been attracting high attention to the application of SCs in electric vehicles, renewable energy sources, and wearable technologies and in a full generation of all-in-one portable electronic devices.[9,10] Their superior performance of SCs is associated with their taking advantage of the combination of batteries and energy storage mechanisms of electrolytic capacitors during their operation. SCs are formed by two electrodes separated by non-conductive, but highly permeable, material. This separator is filled with an electrolyte doped with charges ready to chemically react with the electrode-coating material (as batteries) or to attach to the electrode surface (as electrolytic capacitors) during the charging process. In the first case, the energy storage device is called a pseudocapacitor and, in the second case, it is called an electric double-layer capacitor (EDLC).[10,11]

Recently, transition metal hexacyanoferrates (MHCFs) are known for their high redox behavior and found applications in several areas, such as electrochemical sensors,[12,13] batteries,[14] and supercapacitors.[15,16] Their unique structure, porosity, and high chemical stability make this material especially suitable for use in energy storage devices.[17] Anna Lisowaka-Oleksiak *et al.*[18] prepared a metal hexacyanoferrate network inside a polymer matrix for electrochemical capacitors with high capacitance, which resulted from the presence of inorganic networks.

So far, numerous kinds of MHCFs synthesized by different methods and fabricated on various base electrode materials have been reported, such as NiHCF,[19] CuHCF,[20] MnHCF,[21] CoHCF,[19,22] *etc.* However, there have been no reports on the electrochemical behaviors of NiHCF on carbon cloth electrodes for SC applications. Although the electrochemical behaviors of MHCFs might be similar, it is still essential to examine such electroactive materials because the formation of MHCFs on

---

[a] *Laboratory of Experimental and Applied Physics, Centro Federal de Educação Tecnológica Celso Suckow da Fonseca, Av. Maracanã 229, Rio de Janeiro, 20271-110, Brazil. E-mail: ryesbabu@gmail.com*

[b] *Department of Chemistry, Saveetha Engineering College, Thandalam, Chennai-602 105, Tamil Nadu, India*

electrode surfaces, as well as their electrochemical behaviors, may be different under different conditions.

In this work, we demonstrated a simple and low-cost synthesis of PNHCF-NP. The nanostructured material was characterized by UV-Vis, FTIR, Raman, XRD, XPS, FESEM, EDS, and TEM analysis. The electrochemical performance of the prepared PNHCF-NPs@CC was examined by electrochemical methods, such as cyclic voltammetry, galvanostatic charge–discharge (GCD), and electrochemical impedance spectroscopy (EIS). To the best of our knowledge, the use of carbon cloth as electrode substrate for the PNHCF-NPs deposition may improve the retention of charges during charging as the carbon cloth presents high porosity and good absorption, which imparts characteristics that are close to electrolytic capacitors for the manufactured electrodes.

2. Experimental

2.1. Chemicals

Carbon Cloth was purchased from Sainergy Fuel Cell India Pvt. Ltd. India. Potassium hexacyanoferrate, nickel nitrate, and potassium nitrate were procured from Sigma-Aldrich, USA. All other chemicals were analytical grade and used without further purification. All aqueous solutions were prepared with doubly distilled water.

2.2. Methods

FTIR spectroscopy was performed using the Agilent Cary 630 FTIR spectrometer. Absorption spectra were analyzed with a SHIMADZU UV-2600i UV-Vis spectrophotometer. X-ray diffraction (XRD) analysis was performed on a Bruker model D8 using Cu Kα radiation. Morphology and size of the PNHCF-NPs were studied using FESEM (Model: Quattro S, Singapore); TEM images were obtained using a Hitachi, H7650 Microscope. Electrochemical characterization was performed on a multi-potentiostat (IVIUM Technologies) and a regular three-electrode cell was set up with Ag/AgCl, Pt mesh, and PNHCF-NPs electrodes as reference, counter, and working electrodes, respectively. All experiments were carried out at room temperature and ambient conditions. Two different electrolytes (Na_2SO_4 and K_2SO_4) were utilized and their performances were compared.

2.3. Preparation of potassium nickel hexacyanoferrate nanoparticles (PNHCF-NPs)

PNHCF-NPs were prepared through the drop-wise addition of an aqueous solution of $NiCl_2$ (70 mL of 10 mM solution) to $K_3Fe(CN)_6$ (70 mL of 50 mM solution) containing KCl (50 mM) while stirring.[12] Once the addition finished, the mixture was strongly stirred for a few minutes and then filtered through a 0.4 μm Millipore cellulose filter paper. The precipitate was continuously washed with distilled water and then collected. After filtration, the precipitate was dried overnight at ambient temperature to obtain a powdered material.

2.4. Electrode preparation

The working electrode was fabricated as follows. The as-prepared electroactive material (PNHCF-NPs), activated carbon

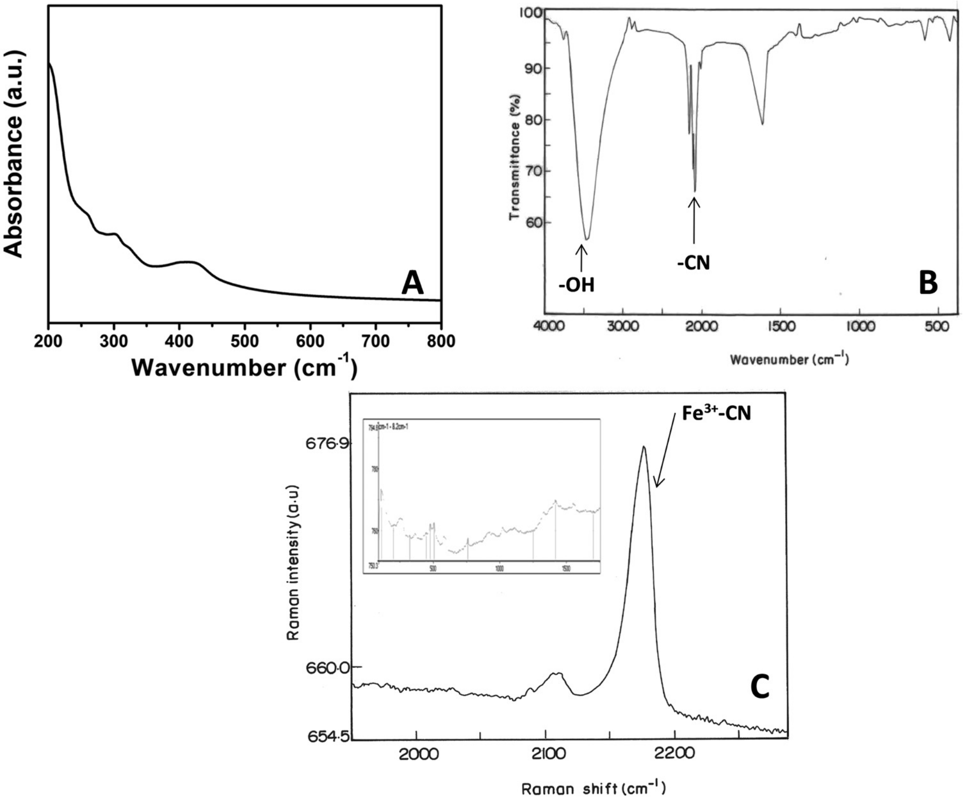

Fig. 1 (A) UV-Vis, (B) FTIR, and (C) Raman spectra of PNHCF-NPs.

(AC), and polyvinylidene fluoride (PVDF) (as a binder) were mixed in a mass ratio of 8 : 1 : 1 and dissolved in *N*-methyl-2-pyrrolidone (NMP). The purpose of the binder is to keep the active material attached to the electrode in the electrolyte solution. The prepared mixture was pasted onto 1 cm × 1 cm carbon cloth, followed by drying at 100 °C for 12 hours. The mass loading of electroactive materials on the carbon cloth was $\sim$2 mg cm^{-2}. According to eqn (1), the specific capacitance (Cs) of the prepared samples was determined from the GCD curve.

$$Q = I \times t/m \times \Delta V \tag{1}$$

where I is the applied current (A); m is the mass of the active material (g); ΔV is the potential range (E), and t is the discharge time (s).

3. Results and discussion

3.1 Physical characterization of PNHCF-NPs

The UV-Vis spectrum of PNHCF-NPs presented strong absorbance at 300 nm and a broad absorption peak at $\sim$413 nm (Fig. 1A). The absorption at 300 nm can be assigned to the ligand to metal charge transfer (LMCT) band of [Fe^{III}(CN)$_6$], and that at 413 nm is due to the d-d transitions of Ni^{II} of PHCFNP. This observation is consistent with earlier reports,[23] which indicate the formation of PNHCF-NPs.

The FTIR spectrum of the PNHCF-NPs is shown in Fig. 1B. The band at 2097 cm^{-1} was attributed to the bridging cyanide (–CN) ligand, offering direct evidence that the bridged dinuclear (Ni, Fe) species were present in the complex. The data was also in agreement with the spectrum obtained by Neff for PB.[24] Two peaks at 594 and 439 cm^{-1} corresponded to the stretching mode of ν(M–C) and bending mode of δ(M–CN), respectively.[25] A broad band around 3444 cm^{-1} indicated the stretching vibrations of the hydroxyl (–OH) group, indicating that the interstitial or zeolitic water present in the complex, which resulted from the association of water molecules due to the H-bonding; this is similar to the absorption exhibited by PB.[24]

The oxidation states of PNHCF-NPs can be determined using Raman spectroscopy. In the Raman spectrum of PNHCF-NPs that are shown in Fig. 1C, it can be observed that the cyanide stretching modes are sensitive to the oxidation state of the coordinating iron. An intense band at 2175.8 cm^{-1} was attributed to the cyanide groups coordinated to Fe (III), indicating that the iron centers were mainly in the Fe^{3+} state. This observation is consistent with earlier reports.[26] At low frequencies, the typical bands related to coordinated Fe (ν-(Fe–N) = 505 cm^{-1}, δ(Fe–C–N) = 441 cm^{-1}, δ(Fe–C–N) = 244.3 cm^{-1} and coordinated Ni (ν_1(Ni–N) = 490 cm^{-1}, (ν_2(Ni–N) = 537 cm^{-1}, δ(N–Ni–N) = 432 cm^{-1}, δ_1(N–Ni–N) = 194 cm^{-1} and δ_2(N–Ni–N) = 268 cm^{-1}, modes were also observed as shown in the inset of Fig. 1C.

Fig. 2 shows the XRD analysis of NiHCF-NPs, which was used to demonstrate the crystallinity of nanoparticles. Peaks were observed at 17.4°, 24.7°, 35.1°, and 39.4°, which could correspond to the diffractions of (200), (220), (400), and (420) planes respectively, demonstrating the face-centered cubic (fcc) structure of NiHCF; the peak positions were similar to NiHCF pattern (JCPDS card, file no. 750037).[12] The XRD peaks were broad and represented the presence of crystallites of nanometer dimensions. The average crystalline size, which was obtained from the half-width of the diffraction peaks by the Debye–Scherrer equation, was found to be $\sim$20 nm.

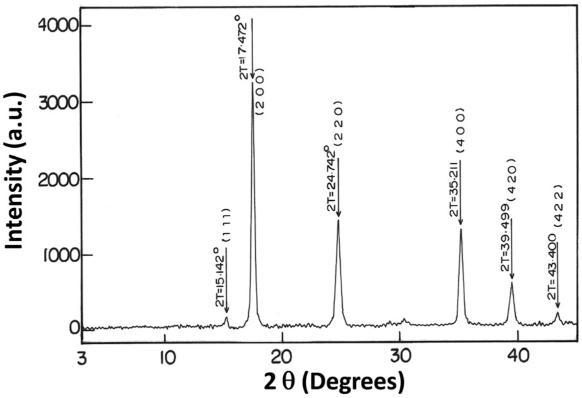

Fig. 2 XRD spectrum of PNHCF-NPs.

The PNHCF-NP complex was also characterized using the XPS technique to confirm the presence of different elements and their oxidation states. Fig. 3A presents the XPS elemental survey scans of the PNHCF-NPs. The Ni 2p peak was observed at 856.2 eV and 874.02 eV confirming the presence of Ni 2p$_{3/2}$ and Ni 2p$_{1/2}$ of Ni (II) species (Fig. 3B).[27,28] The high-resolution XPS of Fe 2p exhibited two peaks at 708.5 eV and 721.4 eV, corresponding to Fe 2p$_{3/2}$ and Fe 2p$_{1/2}$ of Fe^{2+}, respectively (Fig. 3C). The peaks at 710.0 and 723.5 eV (Fig. 3C) could be assigned to Fe 2p$_{3/2}$ and Fe 2p$_{1/2}$, corresponding to Fe (III) species, respectively.[29–31] The XPS peaks observed at 284.5, 398.0, and 532.2 eV showed the presence of C, N, and O in the sample, which is in agreement with earlier reports.[32]

FESEM studies of PNHCF-NPs were carried out to understand the shape and size of the nanoparticles. The corresponding FESEM showed the presence of PNHCF-NPs with spherical morphology and the size distribution ranged between 20–50 nm (Fig. 4A). It can be seen that the average size of the PNHCF-NPs was <50 nm. The size and shape of the nanoparticles were also characterized and confirmed by HRTEM. The image depicts a uniform distribution of PNHCF-NPs. It indicates the formation of PNHCF-NPs with a sphere-like structure, and the size of each nanoparticle was found to be approximately 30 to 50 nm as shown in Fig. 4B. To identify the elemental composition of the PNHCF-NPs, EDS measurement was carried out. The corresponding spectra are shown in Fig. 4C. The appearance of the K, C, N, Ni, and Fe peaks confirms the existence of these elements in the PNHCF-NPs. The amount of Fe atoms is almost equal to the amount of Ni atoms. The proposed empirical formula of the PNHCF-NPs may be written as KNi[Fe(CN)$_6$]. Therefore, the results suggest that alkali metal cations are present in the PNHCF-NPs.

3.2. Electrochemical characterization of PNHCF-NPs

The electrochemical performance of PNHCF-NPs electrodes was evaluated by cyclic voltammetry, galvanostatic charge–discharge

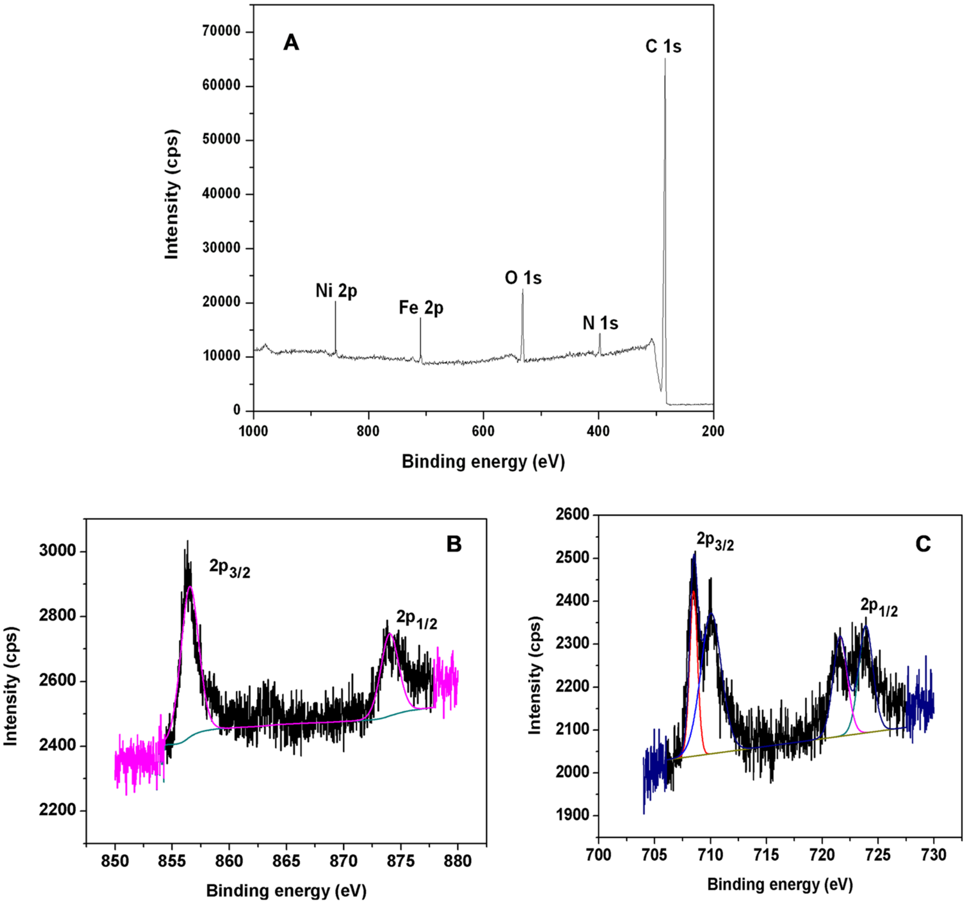

Fig. 3 (A) XPS survey scan of PNHCF-NPs, (B) $2p_{3/2}$ and $2p_{1/2}$ peaks of Ni(II), and (C) $2p_{3/2}$ and $2p_{1/2}$ peaks of Fe(III).

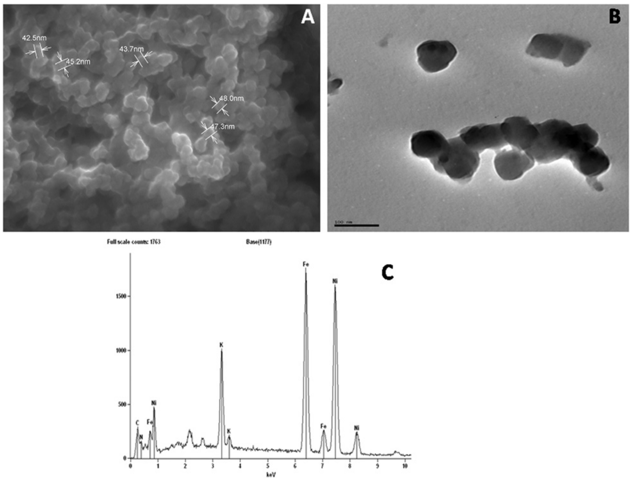

Fig. 4 (A) FESEM, (B) HRTEM images, and (C) EDS spectrum of PNHCF-NPs.

(GCD), and electrochemical impedance spectroscopy (EIS). The cyclic voltammograms (CV) of the PNHCF-NPs electrode were examined at various sweep rates using two different electrolytes, such as aqueous solution of 1 M Na_2SO_4 and 1 M K_2SO_4 as shown in Fig. 5A and B. Cyclic voltammetry is a suitable method to evaluate the capacitive behavior of the electrode materials. As seen from Fig. 5A and B, the CVs of the PNHCF-NPs electrodes were cycled between voltage ranges: 0 to 1.0 V *vs.* Ag/AgCl in Na_2SO_4 and K_2SO_4 electrolytes. During the scans, reduction and oxidation peaks were observed; ferricyanide, $Fe[(CN)_6]^{4-}$/$(Fe[(CN)_6]^{3-})$, was formed at the surface of the PNHCF during cycling in the Na_2SO_4/K_2SO_4 aqueous solutions. The CV profiles demonstrated a typical pseudo-capacitance behavior through the appearance of a pair of redox peaks with the scanned potential for different scan rates as shown in Fig. 5A and B. The general electrochemical reaction mechanism for the PNHCF-NPs electrode in the Na_2SO_4 (or K_2SO_4) electrolyte was as follows:

$$M_2Ni^{II}[Fe^{II}(CN)_6 \leftrightarrow MNi^{II}[Fe^{III}(CN)_6 + e^- + M^+$$
$$M = K \text{ or } Na$$

The charge–discharge (CD) characteristics of the NHCF-NP in the 1-M Na_2SO_4 and 1-M K_2SO_4 electrolytes were investigated using chronopotentiometry from 0.2 to 0.6 V at various current densities. The corresponding results are shown in Fig. 6A and B, respectively. With the Na_2SO_4 electrolyte, the CD curve deviated in a non-linear fashion during charging, whereas it remained linear with the K_2SO_4 electrolyte. The curves presented large deviations, demonstrating that the capacitance was mainly governed by the redox reactions of MHCF. With increasing current densities from 1 A g^{-1} to 20 A g^{-1}, a very

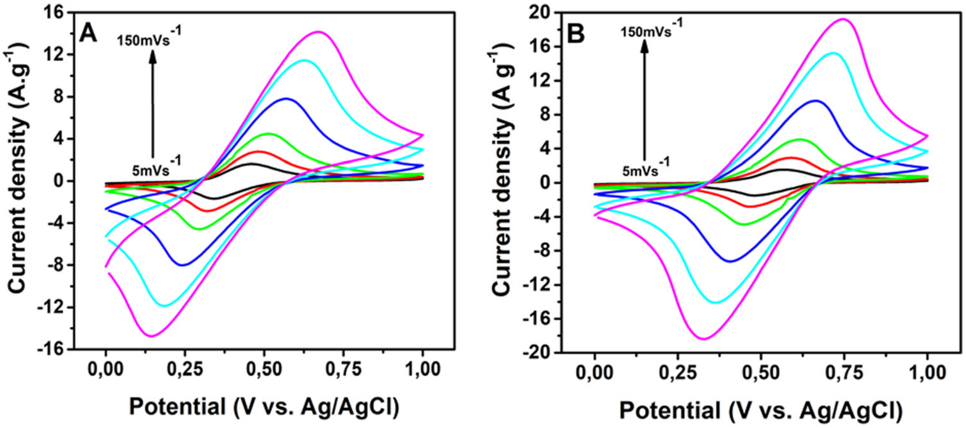

Fig. 5 CVs of PNHCF-NPs electrode at different scan rates from 5, 10, 20, 50, 100, and 150 mV s^{-1}. (A) Na_2SO_4 electrolyte and (B) K_2SO_4 electrolyte.

small drop in the IR in higher current densities was obtained. The specific capacitances were calculated from GCD curves. The capacitances for the electrodes in both electrolytes were calculated using eqn (1). NHCF-NPs@CC electrode in the Na_2SO_4 electrolyte presented higher specific capacitances than the same electrode in the K_2SO_4 electrolyte, and their optimum performance was 198.6 F g^{-1} and 168.8 F g^{-1} at a current density of 0.4 A g^{-1} as shown in Fig. 7A and B. It is important to note that the NHCF-NPs@CC in Na_2SO_4 and K_2SO_4 electrolytes showed good specific capacitance retention value with an increase in the current density (from 0.4 to 4 A g^{-1}). A comparison of the specific capacitances obtained for NHCF-NPs@CC in both electrolytes is summarized in Table 1.

The long-term stability of the fabricated PNHCF-NPs@CC electrode was evaluated using the GCD method. The specific capacitances obtained from the GCD profiles in Na_2SO_4 and K_2SO_4 electrolytes are shown in Fig. 8A and B, respectively. As seen from the Figure, the PNHCF-NPs@CC electrode exhibited

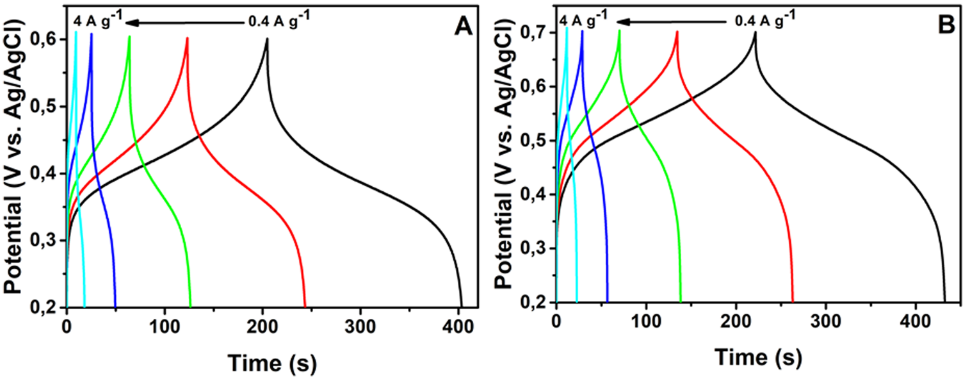

Fig. 6 Galvanostatic charge–discharge curves of PNHCF-NPs electrode. (A) Na_2SO_4 electrolyte and (B) K_2SO_4 electrolyte.

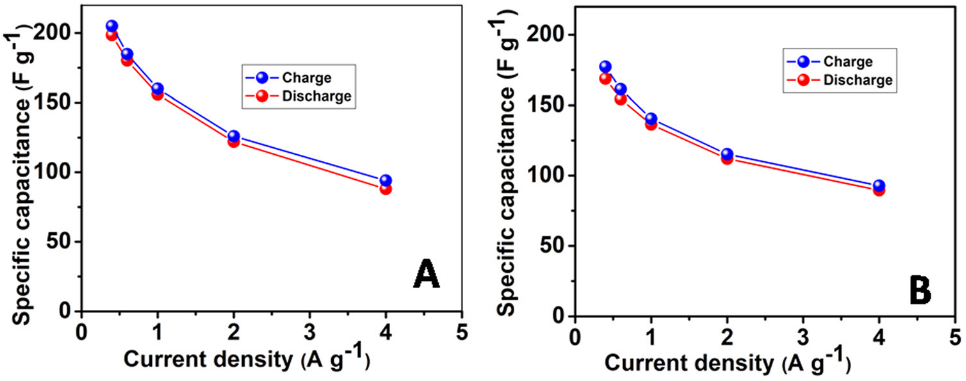

Fig. 7 Specific capacity of the electrodes at different current densities in (A) Na_2SO_4 electrolyte and (B) K_2SO_4 electrolyte.

Table 1 Comparison of the specific capacitance (F g^{-1}) of PNHCF-NPs in different electrolytes

Current density (A g^{-1})	Na_2SO_4 (F g^{-1})	K_2SO_4 (F g^{-1})
0.4	198.6	168.6
0.6	180.3	154.32
1	156	136.4
2	122	112
4	88	89.6

high stability with a small decrease in the capacitance and charge storage after 1000 cycles in both electrolytes. The specific capacitance of the electrode initially decreased and then became almost constant. After 1000 cycles, the capacitance decreased by only ~6% of the initial capacitance, demonstrating outstanding cycle stability. This indicates that the repetitive cycling in either the Na_2SO_4 or K_2SO_4 electrolyte does not induce noticeable degradation of the PNHCF-NPs structure. This high stability over long cycles demonstrates that the fabricated electrode is suitable for practical applications.

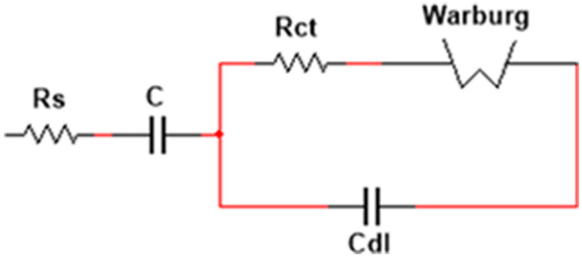

Fig. 10 Equivalent circuit obtained from the system frequency response.

The behavior of the electrodes was also analyzed using EIS with both the electrolytes at the formal potential in the frequency range from 1 GHz to 1 Hz. The frequency response of each electrode/electrolyte system allowed the corresponding Nyquist curve to be plotted (Fig. 9). The correct interpretation of the obtained results allowed the assembly of an equivalent electrical circuit and allowed the description of the same behavior of the electrode/electrolyte system. The beginning of the curve illustrates the resistance of the electrolyte (R_s). In this paper, the R_s were considered to be both ohmic resistances, electrolyte, and internal resistance from the electrode materials, instead of only the electrolyte resistance (as is usually done); otherwise, the resistance would be the same for both experiments, given that the same electrolyte was utilized. The semicircle in the high-frequency region was associated with the charge transfer resistance (R_{ct}), combined with two capacitors,

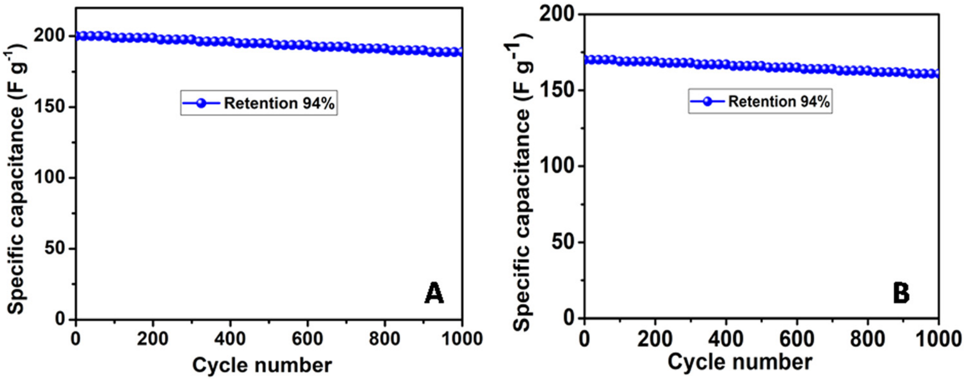

Fig. 8 Long-term cycling stability of the PNHCP-NPs@CC electrode at current density of 0.4 A g^{-1} in the (A) Na_2SO_4 electrolyte and (B) K_2SO_4 electrolyte.

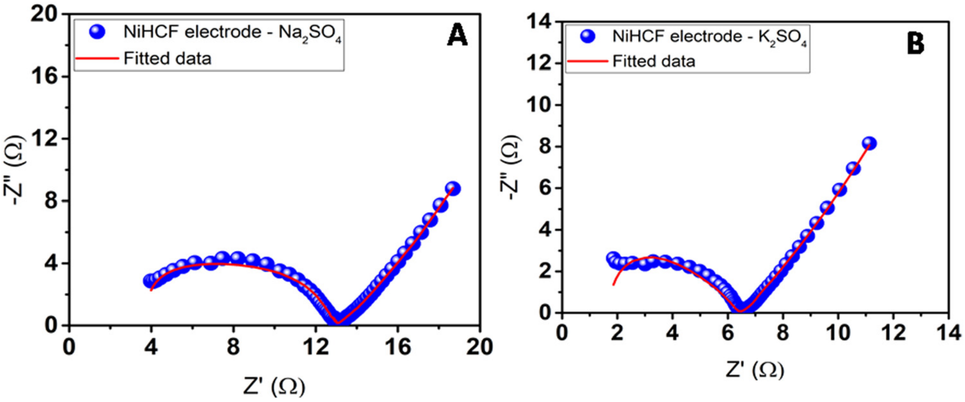

Fig. 9 Nyquist plots for the coated PNHCF-NPs electrode with (A) Na_2SO_4 electrolyte and (B) K_2SO_4 electrolyte.

Table 2 Fitting data of equivalent circuit elements obtained from the frequency response

Electrolyte	R_s (Ω)	R_{ct} (Ω)	$C_1 \times 10^{-6}$ (F)	$C_2 \times 10^{-3}$ (F)	W (Ω^{-1})
Na_2SO_4	3.42	0.32	0.108	598.9	149.8
K_2SO_4	0.93	5.37	0.136	475.9	188.9

that represents the capacity of the material. Its diameter often represents the resistance of the electrode material, combined with the resistance of the coated material and the current collectors. The diffusion of the ions is represented as straight lines in medium frequencies and can be described by the Warburg element (W). The equivalent circuit and respective values are shown in Fig. 10 and summarized in Table 2. It can be noted that the initial resistance is lower for K_2SO_4. The good conductivity of carbon cloth also contributes to the low resistance value for both electrodes. The experiment with Na_2SO_4 electrolyte also presents higher resistance (R_{ct}) compared to that with K_2SO_4; this difference is likely associated with higher ionization energy.

4. Conclusions

In summary, PNHCF-NPs with a spherical structure were successfully prepared by a low-cost and convenient co-precipitation method. The PNHCF-NPs were physically characterized by various methods, such as UV-Vis, FTIR, XPS, FESEM, and EDS. The PNHCF-NPs thus obtained play an important role in ion insertion/desertion and electrolyte access. The electrochemical measurements were performed using two different electrolytes, namely, Na_2SO_4 and K_2SO_4, employing cyclic voltammetry, GCD, and EIS techniques. The high specific capacitances of the PNHCF-NPs@CC electrode of 198.6 F g^{-1} in Na_2SO_4 electrolyte and 168.8 F g^{-1} in the K_2SO_4 electrolyte were obtained at 0.4 A g^{-1}, excellent rate performance of 88 F g^{-1} (Na_2SO_4) F g^{-1} and 89 F g^{-1} (K_2SO_4) were recorded even at 4 A g^{-1}. It was found that the PNHCF-NPs@CC electrode was more electrochemically stable at up to 1000 GCD cycles in the Na_2SO_4 and K_2SO_4 electrolytes.

Conflicts of interest

There are no conflicts to declare.

Acknowledgements

Dr R. S. Babu wishes to acknowledge the Coordenação de Aperfeiçoamento de Pessoal de Nível Superior (CAPES) for financial support (88887.798322/2022-00) and Fundação de Amparo à Pesquisa do Estado do Rio de Janeiro (FAPERJ) for the financial support of the senior post-doctoral fellow (E-26/202.333/2021). Prof. A. L. F. de Barros wishes to acknowledge the Conselho Nacional de Desenvolvimento Científico e Tecnológico (CNPq) (301868/2017-4 and 407938/2018-4), the Financiadora de Estudos e Projetos (FINEP) (0647/18), and FAPERJ (E-26/210.965/2021, E-26/210.801/2021, E-26/245.307/2019, and E-26/241.202/2018) for partial support. This research work was also funded in part by the Coordenação de Aperfeiçoamento de Pessoal de Nível Superior - Brazil (CAPES) under Finance Code 001.

References

1 S. Fiorenti, J. Guanetti, Y. Guezennec and S. Onori, Modeling and experimental validation of a hybridized energy storage system for automotive applications, *J. Power Sources*, 2013, **241**, 112–120.
2 D. Iannuzzi and P. Tricoli, Speed-based state-of-charge tracking control for metro trains with onboard supercapacitors, *IEEE Trans. Power Electron.*, 2012, **27**, 2129–2140.
3 C. Li, Q. Zhang, J. Sun, T. Li, E. Songfeng, Z. Zhu, B. He, Z. Zhou, Q. Li and Y. Yao, High-performance quasi-solid-state flexible aqueous rechargeable Ag–Zn battery based on metal-organic framework-derived Ag nanowires, *ACS Energy Lett.*, 2018, **3**, 2761–2768.
4 Q. Zhang, C. Li, Q. Li, Z. Pan, J. Sun, Z. Zhou, B. He, P. Man, L. Xie, L. Kang, X. Wang, J. Yang, T. Zhang, P. P. Shum, Q. Li, Y. Yao and L. Wei, Flexible and high-voltage coaxial-fiber aqueous rechargeable zinc-ion battery, *Nano Lett.*, 2019, **19**, 4032–4035.
5 Z. Shen, L. Luo, C. Li, J. Pu, J. Xie, L. Wang, Z. Huai, Z. Dai, Y. Yao and G. Hong, Stratified zinc-binding strategy toward prolonged cycling and flexibility of aqueous fibrous zinc metal batteries, *Adv. Energy Mater.*, 2021, **11**, 2100214.
6 Z. Shen, Z. Tang, C. Li, L. Luo, J. Pu, Z. Wen, Y. Liu, Y. Ji, J. Xie, L. Wang, Y. Yao and G. Hong, Precise proton redistribution for two-electron redox in aqueous zinc/manganese dioxide batteries, *Adv. Energy Mater.*, 2021, **11**, 2102055.
7 P. Thounthong, Model based-energy control of a solar power plant with a supercapacitor for grid-independent applications, *IEEE Trans. Energy Conversion*, 2011, **26**, 1210–1218.
8 N. S. Noorasid, F. Arith, A. N. Mustafa, M. A. Azam, S. Mahalingam, P. Chelvanathan and N. Amin, Current advancement of flexible dye sensitized solar cell: A review, *Optik*, 2022, **254**, 168089.
9 A. Gee, F. Robinson and R. Dunn, Analysis of battery lifetime extension in a smallscale wind-energy system using supercapacitors, *IEEE Trans. Energy Conversion*, 2013, **28**, 24–33.
10 G. Wang, L. Zhang and J. Zhang, A review of electrode materials for electrochemical supercapacitors, *Chem. Soc. Rev.*, 2012, **41**, 797–828.
11 X. Peng, L. Peng, C. Wu and Y. Xie, Two dimensional nanomaterials for flexible supercapacitors, *Chem. Soc. Rev.*, 2014, **43**, 3303–3323.
12 R. S. Babu, P. Prabhu and S. S. Narayanan, Selective electro-oxidation of uric acid in presence of ascorbic acid at a room temperature ionic liquid/nickel hexacyanoferarrate nanoparticles composite electrode, *Colloids Surf., B*, 2011, **88**, 755–763.
13 R. S. Babu, P. Prabhu and S. S. Narayanan, Electrocatalytic oxidation of acetaminophen using 1-ethyl-3-methylimidazolium tetrafluoroborate-nickel hexacyanoferrate nanoparticles

gel modified electrode, *J. Chem. Pharm. Res.*, 2012, **4**, 3592–3600.

14 C. D. Wessells, R. A. Huggins and Y. Cui, Copper hexacyanoferrate battery electrodes with long cycle life and high power, *Nat. Commun.*, 2011, **2**, 550.

15 J. Chen, K. Huang and S. Liu, Insoluble metal hexacyanoferrates as supercapacitor electrodes, *Electrochem. Commun.*, 2008, **10**, 1851–1855.

16 Y. Wang, Y. Yang, X. Zhang, C. Liu and X. Hao, One-step electrodeposition of polyaniline/nickel hexacyanoferrate/sulfonated carbon nanotubes interconnected composite films for supercapacitor, *J. Solid State Electrochem.*, 2015, **19**, 3157–3168.

17 N. K. A. Venugopal and J. Joseph, Electrochemically formed 3D hierarchical thin films of cobalt-manganese (Co-Mn) hexacyanoferrate hybrids for electrochemical applications, *J. Power Sources*, 2016, **305**, 249–258.

18 A. Lisowska-Oleksiak and A. P. Nowak, Metal hexacyanoferrate network synthesized inside polymer matrix for electrochemical capacitors, *J. Power Sources*, 2007, **173**, 829–836.

19 M. A. Maier, R. S. Babu, D. M. Sampaio and A. L. F. de Barros, Binder-free polyaniline interconnected metal hexacyanoferrates nanocomposites (Metal = Ni, Co) on carbon fibers for flexible supercapacitors, *J. Mater. Sci.: Mater. Electron.*, 2017, **28**, 17405–17413.

20 X. Li, A. Wu, C. Gao, Z. K. Li and S. W. Lee, Copper hexacyanoferrate as a long-life cathode for aqueous aluminum ion batteries, *Mater. Today Energy*, 2023, **31**, 101205.

21 R. S. Babu, A. L. F. de Barros, M. A. Maier, D. M. Sampaio, J. Balamurugan and J. H. Lee, Novel polyaniline/manganese hexacyanoferrate nanoparticles on carbon fiber as binder-free electrode for flexible supercapacitors, *Composites, Part B*, 2018, **143**, 141–147.

22 F. Zhao, Y. Wang, X. Xu, Y. Liu, R. Song, G. Lu and Y. Li, Cobalt hexacyanoferrate nanoparticles as a high-rate and ultrastable supercapacitor electrode material, *ACS Appl. Mater. Interfaces*, 2014, **6**, 11007–11012.

23 M. Yang, J. Jiang, Y. Lu, Y. He, G. Shen and R. Yu, Functional histidine/nickel hexacyanoferrate nanotube assembly for biosensor applications, *Biomaterials*, 2007, **28**, 3408–3417.

24 D. Ellis, M. Eckhoff and V. D. Neff, Electrochromism in the mixed-valence hexacyanides. 1. Voltammetric and spectral studies of the oxidation and reduction of thin films of Prussian blue, *J. Phys. Chem.*, 1981, **85**, 1225–1231.

25 K. Nakamoto, *Infrared and Raman spectra of inorganic and coordination compounds*, John Wiley & Sons, Inc., New York, 1986.

26 K. M. Jeerage, W. A. Steen and D. T. Schwartz, Charge-density-dependent partitioning of Cs^+ and K^+ into nickel hexacyanoferrate matrixes, *Langmuir*, 2002, **18**, 3620–3625.

27 Y. J. Yang, J. Dong, C. Zhang, X. Ding, Y. Li, H. Ren and F. Guo, Phosphotungstic acid assisted growth of nickel hexacyanoferrate on Ni foam for binder-free supercapacitor electrode, *J. Electroanal. Chem.*, 2021, **895**, 115537.

28 Y. J. Yang, Y. Li, X. Ding, C. Zhang, H. Ren, F. Guo and J. Dong, Synthesis of nickel hexacyanoferrate nanostructure on carbon cloth with predeposited nickel nanoparticles as precursor for binder-free high-performance supercapacitor electrodes, *J. Alloys Compd.*, 2021, **871**, 159510.

29 Y. J. Yang, M. Liu, C. Jiang, P. Yang, N. Wang, S. Chen and Y. Cheng, One-step hydrothermal growth of reduced graphene oxide/nickel hexacyanoferrate nanocomposite on Ni foam for binder-free supercapacitor electrode, *J. Energy Storage*, 2021, **44**, 103462.

30 Y. J. Yang, C. Jiang, N. Wang, S. Chen, Y. Cheng, P. Yang and M. Liu, In situ hydrothermal growth of manganese hexacyanoferrate with Ni foam as the sacrificing template for high-performance asymmetrical supercapacitor, *Ionics*, 2022, **28**, 2957–2966.

31 T. R. I. Cataldi, G. E. D. Benedetto and A. Bianchini, X-ray photoelectron spectroscopic investigation and electrochemistry of polynuclear indium (III) hexacyanoferrate films, *J. Electroanal. Chem.*, 1998, **448**, 111–117.

32 T. Akitsu and Y. Einaga, Structures, magnetic properties, and XPS of one-dimensional cyanide-bridged Cu^{II}–Ni^{II}/Pt^{II} bimetallic assembly complexes, *Inorg. Chim. Acta*, 2007, **360**, 497–505.